Spark plasma sintering of $Ti_xTa_{1-x}C_{0.5}N_{0.5}$-based cermets: Effects of processing conditions on chemistry, microstructure and mechanical properties

By José M. Córdoba*, Ernesto Chicardi, Rosalía Poyato and Francisco J. Gotor

Instituto de Ciencia de Materiales de Sevilla, Centro Mixto CSIC-US, Américo Vespucio 49, 41092 Sevilla, Spain.

by Valentina Medri, Stefano Guicciardi and Cesare Melandri

CNR-ISTEC, Institute of Science and Technology for Ceramics, Via Granarolo 64, I-48018 Faenza, Italy.

Abstract

Nanometric powdered $Ti_xTa_{1-x}C_{0.5}N_{0.5}$-based cermets were fabricated using a mechanically induced self-sustaining reaction and consolidated by spark plasma sintering. Highly dense cermets were obtained, and their chemistry, microstructure and mechanical properties were characterised by X-ray diffraction, scanning electron microscopy, image analysis, microindentation and nanoindentation. The microhardness was found to depend directly on the contiguity and size of the ceramic hard particles. The samples synthesised at the lowest temperature (1150 ºC) exhibited more homogeneous microstructures and smaller ceramic particles and the best combination of microhardness and fracture toughness.

Keywords: solid state reaction, milling, microstructure, ceramic matrix composite, spark plasma sintering

1. Introduction

The hard material constituents of cermets consist of titanium carbonitride, Ti(C,N), as the principal component, and additional metal carbides of the VB and/or VIB groups, such as VC, NbC, TaC, Mo_2C and WC. A metal binder phase of nickel, cobalt or nickel-cobalt provides the desired adhesion of the hard particles and the required toughness. During the liquid phase sintering process, the hard particles develop a typical core-rim structure, where the core consists of the original undissolved Ti(C,N) particles, and the rim consists of a newly formed complex carbonitride solid solution containing Ti and other transition metals [1-2]. The compositions of the different constituents, and the interactions between them, largely determine the properties of the resulting cermet, such as its elasticity, hardness, fracture strength and oxidation resistance. It has been suggested that using carbonitride solid solutions as raw materials by incorporating most of the transition metal components into a single phase [3-5] can enhance the properties of cermets [6-8]. Moreover, refining the hard particles to a submicrometric or even nanometric level has also been recommended when enhanced strength and shock resistance are required combined with high wear resistance [9].

Fully dense nanostructured bulk materials exhibit enhanced physical and mechanical properties [10]; therefore, these materials are critically important in various fields of materials engineering. The major challenge in fabricating these finished parts involves the retention of the nanograin microstructure following the required sintering from nanoscaled powders. However, typical consolidation techniques inevitably lead to grain growth and make it very difficult to produce cermets with small grain sizes, e.g., below 0.2 μm.

Spark plasma sintering (SPS) has been attracting the attention of many researchers [11-13] because it is a process by which fine grained materials can be

fabricated by sintering powders to their full density at low temperatures within a few minutes [14,15]. The advantage offered by this process is related to its significant features that include the use of high heating rates and high pressures, and the effect of the current or electric discharge on mass transport [16-18]. There is currently a growing interest in extending these results to non-oxide ceramics and cermets that are difficult to sinter, especially titanium carbonitrides [12,19,20].

Recently, the mechanochemical process of a mechanically induced self-sustaining reaction (MSR) has been proposed as a reliable and easy method for obtaining quaternary mixed carbonitrides of titanium and at least one element from the IVB and VB groups [4, 5]. Furthermore, MSR enables these complex carbonitrides to be produced in a short time with high stoichiometric control and nanometric characteristics. Therefore, MSR could be a useful method in practice because it enhances cermet properties via the two aforementioned approaches: the use of carbonitride solid solutions and nanoscaled powders. However, the question of suitable consolidation must also be addressed. The aim of this work was to couple MSR and SPS to produce cermets based on titanium-tantalum carbonitride solid solutions. The densification behaviour of these cermets was investigated, and their chemistry and microstructure were associated with their mechanical properties.

2. Materials and Methods

In this work, MSR was used to synthesise the following materials into powdered cermets: titanium (99% pure, <325 mesh, Strem Chemicals), tantalum (99.9% pure, <325 mesh, Aldrich), graphite (11 m^2/g, Fe≤0.4%, Merck), cobalt (99.8% pure, Strem Chemicals) and high-purity nitrogen gas (H_2O and O_2 ≤3 ppm, Air Liquide). In this method, the strongly exothermic character of the formation of titanium carbonitride

from its elements was exploited to promote self-propagating reactions during the milling process. Elemental Ti-Ta-C-Co powder mixtures with different Ti/Ta atomic ratios (given by the nominal compositions in Table I) were ball-milled under a nitrogen gas pressure of 0.6 MPa using a modified planetary ball mill (model Micro Mill Puverisette 7, Fritsch), enabling the ignition of the self-propagating reactions to be detected [5]. The critical milling time required to ignite the mixture is called the ignition time. Seven tempered steel balls and 6 g of powder were placed in a tempered steel vial (67 HRC) in each milling experiment and milled at 600 rpm. The vial volume was 50 cc. The diameter and mass of the balls were 15 mm and 13.41 g, respectively. The powder-to-ball mass ratio (PBR) was 1/15.65. The ignition times were determined from the time-pressure records and similar values were obtained for all of the mixtures, approx. 40-42 minutes. The milling was prolonged after ignition during 30 minutes to get a better homogenised powder.

The powders were then sintered using SPS equipment (Model-515S, Dr. Sinter Inc., Kanagawa, Japan) at different temperatures and a constant pressure of 30 MPa for different dwell times (see Table I). The temperature was measured using an optical pyrometer focused on a hole in the middle part of the graphite die. For each SPS experiment, 4 g of material were introduced into a cylindrical graphite die with an internal diameter of 15 mm. The compact was lined with a graphite foil to protect the die/plungers and facilitate sample release after sintering. The tests were carried out under vacuum at a heating rate of 200 ^{o}C min^{-1} to reach the maximum temperature.

X-ray diffraction diagrams were obtained using a Panalytical X'Pert Pro instrument, which was equipped with a θ/θ goniometer using Cu K_{α} radiation (40 kV, 40 mA), a secondary K_{β} filter and an X'Celerator detector. The diffraction diagrams were scanned from 30^{o} to 140^{o} (2θ) at a scanning rate of 0.42^{o} min^{-1}. Rietveld analysis

was used to calculate the lattice parameter and stoichiometry of the carbonitride phases with a Fullprof computer program [21]. The diffracting domain sizes were estimated using the Scherrer equation.

The sintered cermets were sectioned and polished until the mirror effect was obtained; a microstructural characterisation was then carried out using scanning electron microscopy (SEM) with a Hitachi FEG S-4800 microscope. The microstructural parameters were evaluated by image analysis (IA) from the boundary intercepts with test lines on planar sections. The average number of intercepts per unit of length was determined for the ceramic/binder interfaces, $(N_L)_{ceramic/binder}$, and for the ceramic/ceramic grain boundaries, $(N_L)_{ceramic/ceramic}$. These parameters were used to calculate the contiguity of the ceramic particles as follows:

$$C = 2(N_L)_{ceramic/ceramic} / (2(N_L)_{ceramic/ceramic} + (N_L)_{ceramic/binder}),$$

and the mean free path of the binder phase was calculated using the equation below:

$$\lambda = Ø_{ceramic} / (N_L)_{ceramic/binder},$$

where $Ø_{ceramic}$ denotes the mean ceramic particle size, as determined from a particle size distribution study.

Vickers tests were performed at room temperature using a microhardness tester (FM-700, Future-Tech Corp.) with a load of 9.81 N (Hv 1.0) for 15 s. Twelve microindentations were made at different locations on the polished surface and the microhardness was reported as an average of the measured values. The indentation microfracture (IM) method was used to evaluate the fracture toughness (K_{ic}) using the equation given below from Shetty et al. [22]:

$$K_{ic} = (0.03026 * P) / (a/2)*l^{1/2},$$

where *P* denotes the load, *l* denotes the crack length and *a* denotes the length of the diagonal of the indentation.

The nanoindentation tests were performed on the polished surfaces using a commercial nanoindenter (Nano Indenter XPTM, MTS Systems Corporation, Oak Ridge, TN, USA) fitted with a Berkovich diamond tip. A peak load of 5 mN was used to measure the nanohardness and the indentation modulus: at least 350 indentations were made at each position. The indenter was continuously loaded up to the peak load in 15 s and immediately unloaded without a holding time. The nanohardness and the indentation modulus were calculated using the data acquisition software of the nanoindenter (TestWorksTM ver. 4.06A), which is based on Oliver and Pharr's model [23]. A Poisson ratio of 0.3 was used to calculate the Young's modulus. The raw load–displacement data were automatically corrected for the machine compliance and thermal drift by the software. The area function of the indenter tip was calibrated using a standard fused silica specimen before testing.

3. Results and Discussion

3.1. Compositional analysis

Figure 1(a) shows the XRD diagrams of the powdered cermets fabricated by MSR: a cubic structure (Fm3m space group) can be observed from the characteristic reflections corresponding to the ceramic component. The position of these reflections is consistent with the formation of a (Ti,Ta)(C,N) quaternary phase, as has been reported previously [3]. The shift in the XRD reflections (see Fig. 1(a) inset, dotted lines) can be attributed to the variations in the composition of the solid solution, confirming that the stoichiometry of the carbonitride phase can be controlled by adjusting the initial Ti/Ta atomic ratio in the elemental powder mixture [3,24]. The large broadening of the XRD reflections indicates the nanometric microstructure of the carbonitride solid solutions.

However, reflections corresponding to elemental Co are not observed in figure 1(a). Instead, a broad reflection associated with a Ti-Ta-Co alloy is observed. Recall that elemental Co was added to the Ti/Ta/C mixture and was present in the reaction medium during the self-sustaining reaction that produced the carbonitride phase. It has been previously shown that the heat released during carbonitride synthesis can trigger the formation of intermetallic phases during the MSR process [3,24].

Figures 1(b), 1(c) and 1(d) show the XRD diagrams of cermets sintered by SPS under different experimental conditions: the reflections associated with the ceramic carbonitride phase are clearly visible. The lattice parameter and stoichiometry of the carbonitride phase are presented for each cermet in Table II. Good agreement was observed between the nominal composition of the reactants introduced into the milling device and the final hard phase composition after sintering. Moreover, these compositions were similar to those calculated for the powdered materials. These results confirmed that MSR could be used to tailor the final ceramic composition and that the SPS process did not modify the chemical composition of the solid solution in the consolidated cermet. Furthermore, the estimated diffracting domain size showed that the nanometric character of the carbonitride phase persisted through the sintering process.

Figures 1(b), 1(c) and 1(d) exhibit new reflections for the binder phase following sintering that can always be assigned to intermetallic phases of the ternary Ta-Ti-Co system. It is difficult to unambiguously assign intermetallic phases because the structural changes that can be introduced by possible Ti and Ta substitutions. Comparison with available reference diffraction patterns showed that the main phase was a Co_2(Ti,Ta) intermetallic solid solution. The intermetallic phase symmetry corresponded to a cubic structure, with the exception of the samples with the lowest Ta content (i.e., samples 8, 9 and 10), which exhibited a hexagonal structure. The Co-Ta

and Co-Ti phase diagrams [25] show that a hexagonal structure forms preferentially over a cubic phase for 2:1 intermetallics with slightly higher Co-compositions. A 1:1 Co(Ti,Ta) intermetallic phase was also observed for some samples (Table II).

3.2. Densification behaviour

Figure 2 presents the characteristic piston displacement and temperature profiles that were recorded in situ during the SPS experiments. Although the displacement output includes not only the sample shrinkage, but also the thermal expansion of sample, both electrodes, graphite blocks, spacers and plungers, its evolution with time provides valuable information on the densification behaviour of samples.

This figure shows that the sintering process (as characterised by the measurable shrinkage) began around 750ºC for all of the investigated samples. This temperature corresponds to ~0.5 T_m (the melting point temperature) for cobalt, which is the temperature at which appreciable solid state sintering begins, when aided by the applied pressure. Figure 2 shows that cermet densification mainly occurred during the heating step, corresponding to intermediate stage sintering during which the neighbouring sinter necks grow sufficiently large to overlap with each other. By contrast, the shrinkage was low during the short isothermal sintering time.

A clear plateau was not observed in the shrinkage profiles of samples 1 and 2, suggesting that the maximum densification was not achieved because of the short dwell time at 1250 ºC and 1350 ºC, respectively. Prolonging the dwell time at 1350 ºC for samples 3 and 4 resulted in maximum densification of the samples (Fig. 2(a)). These results contrast with the data in figures 2(b) and 2(c), in which samples 6 and 9 attained the shrinkage plateau before reaching the maximum temperature of 1250 ºC. The plateau was observed during the dwell time period for samples 5 and 8, which were only

sintered at 1150 ºC. These contradictory results can be attributed to the difference in the Ta content of the cermets. When the Ta content of the cermets increases, a higher temperature is needed to reach a liquid phase state in the binder that facilitates sintering. It has previously been shown that significantly higher sintering temperatures are required to properly densify cermets with high Ta content [3].

Note that these sintering temperatures are significantly lower than those required to densify cermets with similar compositions by pressureless sintering methods (1475-1550 ºC) [3,24,26,27] but are also relatively lower than the reported temperatures for pressure-assisted methods such as hot pressing [28,29].

3.3. Microstructural characterisation

Figure 3 shows representative SEM micrographs of the polished surfaces of the sintered cermets. The image analysis data are presented in Table III and figure 4. Some cermets, particularly those that were sintered at higher temperatures and for longer times, exhibited a low binder content, which could be attributed to the loss of the molten binder during the SPS process. This loss was due to the extreme difficulty in sealing the sample holder in this type of sintering procedure and because of the high binder fluidity at this temperature and pressure. This hypothesis was verified by the presence of metal outside the graphite sample holder.

All of the cermets exhibited a significantly small ceramic particle size, corresponding to limited growth of the carbonitride grains during the SPS process. Note that the sintering process was very fast and the overall length of the process did not exceed 15 min for any sample. In comparison with previous studies carried out in our lab using similar starting materials but densified by a pressureless technique, a clear decreasing in the ceramic particle size was observed. Using the best sintering

conditions, the average particle size obtained by SPS was ~1 μm instead of ~ 3 μm as found by conventional methods [3,24,27].

Although a large proportion of ceramic particles were in the nanometric and submicrometric ranges, some micrometric ceramic particles were also observed. Most of these micrometric particles (which were most visible in cermets with higher tantalum contents because of the higher image contrast) showed a typical core-rim microstructure (see samples 1, 2, 3 and 5 in fig. 3), providing evidence of grain growth by dissolution-reprecipitation processes despite the short residence time at the maximum sintering temperature. The number of particles with this microstructure increased with the sintering time and temperature.

A general trend can be observed in figures 3 and 4 and Table III, whereby larger ceramic particles and wider size distributions were obtained with increasing sintering temperatures and times, as expected. However, note that this effect was less pronounced when the initial Ta content increased because the grain growth decreased. Figure 4 shows that the cermets with 20 at.% Ta that were sintered for a short time (i.e., samples 1, 2 and 3) had the narrowest ceramic size distributions. In these cases, the most relevant feature of the microstructure was the presence of nanometric and submicrometric carbonitride grains, which were generated during the milling synthesis and were retained in the microstructure because of the fast sintering process. The binder phase was also more homogeneously distributed around the carbonitride grains in these samples. However, these submicrometric carbonitride grains were almost completely absent from the microstructure of cermets that were processed using longer sintering times because the higher dissolution potential of the smaller ceramic grains caused them to dissolve and reprecipitate on the coarser ceramic grains after diffusion through the binder.

Table III and figure 5(a) present the ceramic contiguity and the binder mean free path, which were calculated to compare the samples investigated and rationalise the effects of microstructure on the mechanical behaviour of the samples. The two parameters exhibited an opposite trends, i.e., the contiguity increased and the mean free path decreased with increasing temperatures and sintering times. This behaviour was also related to the cobalt loss during sintering, which affected the final binder content of the cermets. Therefore, smaller mean free paths were observed for cermets with a lower binder content. Increasing the Ta content tended to produce a shorter mean free path because of the smaller size of the ceramic particles.

3.4. Mechanical properties

All of the cermets investigated exhibited high microhardness values, which are summarised in Table III. Figure 5(b) illustrates the effects of the sintering temperature and the ceramic composition on the microhardness. This plot shows that the microhardness was highly dependent on the sintering temperature. Enhanced densification and binder loss with increasing temperature are possible reasons for this behaviour. At 1150 ºC and 1250 ºC, the microhardness was almost constant and therefore independent of the initial composition. However, at 1350 ºC with the same sintering time (8 min), the microhardness increased with the Ta content of the cermets. By comparing figures 5(a) and 5(b), the microhardness was found to be directly and inversely proportional to the ceramic contiguity and the binder mean free path, respectively.

Figure 5(c) is a typical SEM image illustrating the Vickers indentation. The cracks induced at the corners of the Vickers indentation mark propagated along the grain boundary and traversed some large grains, resulting in both inter- and intra-

granular grain failures (fig. 5(d)). The corner crack lengths were used to estimate the indentation fracture toughness using Shetty et al.'s equation, which is summarised in Table III with the K_{Ic} values. The low observed values can be attributed to the presence of an intermetallic phase (as opposed to a tough metal phase) in the binder, which caused binder brittleness. The highest K_{Ic} value for each nominal composition corresponded to the cermet that reached the maximum densification at the lowest temperature in the shortest dwell time (i.e., samples 3, 5 and 8) and which therefore had the highest binder content.

A slight increase in K_{Ic} was observed upon decreasing the Ta content of the initial mixture, even when the binder mean free path decreased because of the presence of larger ceramic particles. Although the fracture toughness was enhanced by the presence of smaller grains (corresponding to samples with higher Ta contents) and strong interfacial bonding among grains, a higher Ta content in the intermetallic solid solution phase (binder) may also have promoted crack propagation because of the increase in the Young's modulus for Ta (186 GPa) relative to the Young's modulus for Ti (116 GPa).

Nanoindentation was used to measure the nanomechanical properties of the cermets (i.e., samples 1, 6 and 9). Figure 6 shows a set of SEM images with typical Berkovich nanoindenter indentation marks. The size of the nanoindentation marks was used to differentiate the nanohardness of the ceramic phase from that of the binder phase. Examining the SEM images also enabled us to determine the Young's modulus and the hardness of each constituent phase. Figure 7 presents representative data for the binder and ceramic phases for every composition. The ceramic component exhibited high nanohardness values ranging from 30 GPa to 35 GPa, whereas the nanohardness of the binder phase ranged between 15 GPa and 23 GPa, depending on the Ta content. The

Young's modulus of the binder was found to range from 375 GPa to 400 GPa. The high modulus and nanohardness of the binder resulted from using an intermetallic solid solution instead of elemental Co; therefore, the binder mechanical properties resembled those of a ceramic material.

The nanoindentation experiments confirmed that both the nanohardness and the Young's modulus of the binder and ceramic phases increased with increasing the Ta content. Recall that Ta was present in both the ceramic and binder phases. However, the resistance to deformation in response to an applied force decreased as the tantalum content increased. That is, both the Young's modulus and the hardness decreased with increasing grain size in accordance with the Hall–Petch relation [30,31]. This result can be observed in figure 6, where a clear increase in the particle size can be observed with a decrease in the Ta content.

In comparison with other reported values for the microhardness and fracture toughness of similar materials (cemented carbides [32,33] or cermets [34]), $Ti_xTa_{1-x}C_yN_{1-y}$+Co sintered materials showed similar microhardness, but lower values of fracture toughness. This low fracture toughness was attributed to the presence of intermetallics in the binder phase, which caused brittleness in the cermets. However, compared to the same type of materials (containing intermetallics in the binder) [27], SPS allowed obtaining higher hardness values (~ 15 GPa instead of 12 GPa) as a direct consequence of a smaller ceramic particle size. Regarding fracture toughness, similar values were found (~ 4.5 $MPam^{1/2}$) because of this property is mainly determined by the nature of the binder phase.

4. Conclusions

A mechanically induced self-sustaining reaction was used to synthesise $Ti_xTa_{1-x}C_{0.5}N_{0.5}$/Co cermets, and the effect of spark plasma sintering conditions on the chemistry, microstructure and mechanical properties of the cermets was investigated. The major conclusions are summarised below.

1. At low Ta contents, densification was possible at temperatures as low as 1150 ºC.
2. Grain growth was limited without adversely affecting high densification. For the best sintering conditions, the average hard component particle size was ~ 1 μm.
3. The microhardness increased with the Ta content of the cermets; this result was confirmed by nanoindentation experiments, which showed that the nanohardness of both the ceramic and binder phases increased with the Ta content.
4. Decreasing the Ta content of the initial mixture resulted in a slight increase in K_{Ic}. The low K_{Ic} values observed for all of the cermets was because of the presence of intermetallic compounds in the binder.

Coupling MSR synthesis with SPS sintering is promising because the nanometric microstructure of the MRS powders can be retained during SPS.

Acknowledgments

This work was supported by the Spanish government under grant No. MAT2011-22981, which is financed in part by the European Regional Development Fund of 2007–2013. E. Chicardi and J. M. Córdoba were supported by CSIC through JAE-Pre and JAE-Doc grants, respectively, which are financed in part by the European Social Fund (ESF). The authors wish to thank Prof. Arturo Domínguez-Rodríguez (Dpto. de Física de la Materia Condensada, Universidad de Sevilla, Spain) for his assistance in SPS experiments.

References

[1] E.T. Jeon, J. Joardar, S. Kang, Microstructure and tribo-mechanical properties of ultrafine Ti(CN) cermets, Int. J. Refract. Met. Hard Mater. 20 (2002) 207–11.

[2] S.Y. Ahn, S. Kang, Formation of core-rim structures in Ti(C, N)–WC–Ni cermets via a dissolution and precipitation process, J. Am. Ceram. Soc. 83(2000) 1489–94.

[3] E. Chicardi, J.M. Córdoba, M.J. Sayagués, F.J. Gotor, Inverse core–rim microstructure in (Ti, Ta)(C,N)-based cermets developed by a mechanically induced self-sustaining reaction, Int. J Refract Met Hard Mater. 31 (2012) 39-46.

[4] J.M. Córdoba, M. A. Avilés, M. J. Sayagués, M. D. Alcalá, F. J. Gotor, Synthesis of complex carbonitride powders $Ti_yM_{T1-y}C_xN_{1-x}$ (M_T: Zr, V, Ta, Hf) via a mechanically induced self-sustaining reaction, J. All. Comp. 482 (2009) 349–355

[5] J.M. Córdoba, M.J. Sayagués, M.D. Alcalá and F.J. Gotor, Monophasic $Ti_yNb_{1-y}C_xN_{1-x}$ nanopowders obtained at room temperature by MSR, J. Mater. Chem. 17 (2007) 650–653

[6] P. Ettmayer, H. Kolaska, W. Lengauer, K. Dreyer, Ti(C,N) cermets-metallurgy and properties, Int. J. Refr. Met. Hard. Mater. 13 (1995) 343–51.

[7] H. Matsubara, Application of hard and ultra-hard materials, J. Jap. Inst. Metals 29[12] (1990)1008–18.

[8] Zhang S, Material development of titanium carbonitride-based cermets for machining application, Key Eng. Mater. 521 (1998) 138–140.

[9] C.C. Koch, Nanostructured Materials. Processing, Properties and Potential Applications, Noyes Publications. Norwich, New York. USA. 2002

[10] R.G. Reddy, Processing of nanoscale materials, Rev. Adv. Mater. Sci. 5 (2003)121–133.

[11] L. Gao, H. Wang, H. Kawaoka, T. Sekino, K. Niihara, Fabrication of YAG–SiC nanocomposites by spark plasma sintering, J. Eur. Ceram. Soc. 22 (2002) 785–789.

[12] Y. Zheng, S.X. Wang, M. You, H.Y. Tan, W.H. Xiong, Fabrication of nanocomposite Ti(C,N)-based cermet by spark plasma sintering, Mater. Chem. Phys. 92 (2005) 64–70.

[13] R. Chaim, Densification mechanisms in spark plasma sintering of nanocrystalline ceramics, Mater. Sci. Eng. A. 443 (2007) 25–32.

[14] K. Ichikawa, T. Murakami, Y. Nakayama, S. Miyamato, M. Tokita, Preparation and mechanical properties of nanocrystalline bulk materials by spark plasma sintering process, Mater. Sci. Forum. 426–432 (2003) 2375–2380.

[15] U. Anselmi-Tamburini, J.E. Garay, Z.A Munir, Fast low-temperature consolidation of bulk nanometric ceramic materials, Scripta Mater. 54 (2006) 823-828

[16] A. Munir, U. Anselmi-Tamburini and M. Ohyanagi, The effect of electric field and pressure on the synthesis and consolidation of materials: A review of the spark plasma sintering method, J Mater Sci. 41 (2006) 763–777

[17] Wang, L., Zhang, J., Jiang, W., Recent development in reactive synthesis of nanostructured bulk materials by spark plasma sintering, International Journal of Refractory Metals and Hard Materials 39 (2913) 103-112

[18] Saheb, N., Iqbal, Z., Khalil, A., Hakeem, A.S., Al Aqeeli, N., Laoui, T., Al-Qutub, A., Kirchner, R.,Spark plasma sintering of metals and metal matrix nanocomposites: A review, Journal of Nanomaterials 2012 (2012) 983470

[19] P. Angerer, L.G. Yu, K.A. Khor, G. Korb, I. Zalite, Spark-plasma-sintering (SPS) of nanostructured titanium carbonitride powders, J. Eur. Ceram. Soc. 25 (2005) 1919–27.

[20] J.M. Córdoba, E. Chicardi, F. J. Gotor, Development of multicomponent–multiphase materials based on (Ti,Ta,Nb)C_xN_{1-x} carbonitride solid solutions, Chem. Eng. J. 192 (2012) 58–66

[21] T. Roisnel and J. Rodríguez-Carvajal, WinPLOTR: a Windows tool for powder diffraction patterns analysis. Mater. Sci. Forum 378-381, (2001) 118-123

[22] D.K. Shetty, I.G. Wright, P.N. Mincer and A.H. Clauer, Indentation fracture of. WC-Co cermets, J. Mater. Sci. 20 (1985) 1873-1882.

[23] W.C. Oliver, G.M. Pharr, An improved technique for determining hardness and elastic modulus using load and displacement sensing indentation experiments, J. Mater. Res.7 (1992) 1564–82.

[24] E. Chicardi, J.M. Córdoba, M.J. Sayagués and F.J. Gotor, Absence of the core-rim microstructure in $Ti_xTa_{1-x}C_yN_{1-y}$-based cermets developed from a pre-sintered carbonitride master alloy, Int. J. Refract. Met. Hard Mater. 33 (2012) 38–43.

[25] ASM Handbook, Volume 3 Alloy Phase Diagrams, ASM International, 1992

[26] S. Park, S. Kang, Toughened ultrafine (Ti,W)(CN)–cermets, Scripta Mater. 52 (2005)129–133

[27] E. Chicardi, Y. Torres, J.M. Córdoba, P. Hvizdoš and F.J. Gotor, Effect of Tantalum content on the microstructure and mechanical behaviour of cermets based on (Ti_xTa_{1-x})($C_{0.5}N_{0.5}$) solid solutions. Mater. Design. Accepted.

[28] F. Monteverde, A. Bellosi, L. Scatteia, Microstructure of hot-pressed Ti(C,N)-based cermets, J. Eur. Ceram. Soc. 485 (2008) 415–421.

[29] J.M. Sánchez, M. Alvarez, N. Rodriguez, M. Aristizabal, Effect of Ni powder characteristics on the consolidation of ultrafine TiMoCN cermets by means of SPS and HIP technologies, Mat. Sci. Eng. A. 500 (2009) 225–232.

[30] H.L. Kyong, I.C. Seung, K.K. Byung et al, Effect of WC/TiC grain size ratio on microstructure andmechanical properties of WC–TiC–Co cemented carbides, Int. J. Refract. Met. Hard Mater. 24 (2006) 109–14.

[31] D. Jia, K.T. Ramesh, E. M,. Effects of nanocrystalline and ultrafine grain sizes on constitutive behaviour and shear bands in iron, Acta Mater. 51 [12] (2003) 3495–3509.

[32] H.-C. Kim, I.-J. Shon, J.-K. Yoon, J.-M. Doh, Consolidation of ultra-fine WC and WC–Co hard materials by pulsed current activated sintering and its mechanical properties, Int. J. Refract. Met. Hard Mater. 25 (2007) 46–52.

[33] S. Zhao, X. Song, C. Wei, L. Zhang, X. Liu., J. Zhang, Effects of WC particle size on densification and properties of spark plasma sintered WC–Co cermet, Int. J. Refract. Met. Hard Mater. 27 (2009) 1014–1018.

[34] Y. Peng , H. Miao, Z. Peng, Development of TiCN-based cermets: Mechanical properties and wear mechanism, , Int. J. Refract. Met. Hard Mater 39 (2013) 78–89

Figure Captions

Figure 1. XRD diagrams for (a) powdered cermets and sintered cermets with ceramic nominal compositions of (b) $Ti_{0.8}Ta_{0.2}C_{0.5}N_{0.5}$, (c) $Ti_{0.9}Ta_{0.1}C_{0.5}N_{0.5}$ and (d) $Ti_{0.95}Ta_{0.05}C_{0.5}N_{0.5}$; (•) $Ti_xTa_{1-x}C_yN_{1-y}$ [Fm3m], (○) $Ti_xTa_{1-x}Co$ [Pm3m], (♦) Ta [Im3m], (*) $Ti_xTa_{1-x}Co_2$ [Fd3m] and (♠) $Ti_xTa_{1-x}Co_2$ [P63/mmc]

Figure 2. Piston displacement and temperature profile as a function of the process time of the SPS experiments for cermets with ceramic nominal compositions of (a) $Ti_{0.8}Ta_{0.2}C_{0.5}N_{0.5}$, (b) $Ti_{0.9}Ta_{0.1}C_{0.5}N_{0.5}$ and (c) $Ti_{0.95}Ta_{0.05}C_{0.5}N_{0.5}$.

Figure 3. Representative SEM images of the polished surface of sintered cermets at (a) low and (b) high magnifications; the arrows indicate micrometric particles with a core-rim microstructure

Figure 4. Particle size distribution of the ceramic phase in sintered cermets

Figure 5. (a) Binder mean free path (□) and ceramic contiguity (△) for different samples, (b) Vickers microhardness for different samples, (c) characteristic SEM image of a microindentation and (d) SEM image of a crack produced by a microindentation

Figure 6. Representative SEM micrographs of cermets showing nanoindentation marks

Figure 7. Nanohardness and Young's modulus as function of the nominal composition; (□ binder, ○ ceramic)

Table I. Nominal composition of cermets synthesised by MSR and experimental conditions for SPS sintering. The milling process was performed under 6 bars of nitrogen gas pressure being the vial connected to the gas supply during all the procedure.

Sample	Nominal Composition	SPS Sintering	
		Temperature	Dwell Time
1	80 wt.% [0.8 Ti; 0.2 Ta; 0.5 C %at.] + 20 wt.% Co	1250 ºC	40 s
2		1350 ºC	40 s
3		1350 ºC	120 s
4		1350 ºC	480 s
5	80 wt.% [0.9 Ti; 0.1 Ta; 0.5 C %at.] + 20 wt.% Co	1150 ºC	120 s
6		1250 ºC	120 s
7		1350 ºC	480 s
8	80 wt.% [0.95 Ti; 0.05 Ta; 0.5 C %at.] + 20 wt.% Co	1150 ºC	120 s
9		1250 ºC	120 s
10		1350 ºC	480 s

Table II. Lattice parameter, stoichiometry and coherent diffraction domain size for the ceramic carbonitride phase and nature of the binder phase in sintered cermets

	Ceramic Phase			Binder Phase	
Sample	**Ceramic Composition**	**a (Å)**	**D [nm]**	**Phase 1**	**Phase 2**
1	$Ti_{0.77}Ta_{0.23}C_{0.51}N_{0.49}$	4.3264	26	$Co_2Ti(Ta)$ [Fd3m]	
2	$Ti_{0.79}Ta_{0.21}C_{0.59}N_{0.41}$	4.3260	34	$Co_2Ti(Ta)$ [Fd3m]	
3	$Ti_{0.81}Ta_{0.19}C_{0.57}N_{0.43}$	4.3267	32	$Co_2Ti(Ta)$ [Fd3m]	
4	$Ti_{0.81}Ta_{0.19}C_{0.58}N_{0.42}$	4.3278	36	$Co_2Ti(Ta)$ [Fd3m]	
5	$Ti_{0.90}Ta_{0.10}C_{0.60}N_{0.40}$	4.3162	33	$Co_2Ti(Ta)$ [Fd3m]	CoTi(Ta) [Pm3m]
6	$Ti_{0.90}Ta_{0.10}C_{0.59}N_{0.41}$	4.3149	44	$Co_2Ti(Ta)$ [Fd3m]	CoTi(Ta) [Pm3m]
7	$Ti_{0.87}Ta_{0.13}C_{0.61}N_{0.39}$	4.3142	64	$Co_2Ti(Ta)$ [Fd3m]	
8	$Ti_{0.97}Ta_{0.03}C_{0.65}N_{0.35}$	4.3017	38	$Co_2Ti(Ta)$ [P63/mmc]	CoTi(Ta) [Pm3m]
9	$Ti_{0.97}Ta_{0.03}C_{0.66}N_{0.34}$	4.3027	51	$Co_2Ti(Ta)$ [P63/mmc]	CoTi(Ta) [Pm3m]
10	$Ti_{0.91}Ta_{0.09}C_{0.63}N_{0.37}$	4.3087	75	$Co_2Ti(Ta)$ [P63/mmc]	CoTi(Ta) [Pm3m]

Table III. Microstructural parameters (ceramic content, binder content, porosity volume, mean ceramic particle size, ceramic contiguity and binder mean free path) and mechanical properties (Vickers hardness and fracture toughness) of sintered cermets

	Image Analysis						Indentation	
Sample	**Ceramic Volume (%)**	**Binder Volume (%)**	**Porosity Volume (%)**	**Mean Ceramic Particle Size (μm)**	**Contiguity**	**Binder Mean Free Path (μm)**	**H_v (1.0) [GPa]**	**K_{Ic} [$MPam^{1/2}$]**
1	80	17	3	0.62	0.36	1.21	14.9	4.2
2	80	16	4	0.85	0.50	1.05	15.7	3.6
3	81	17	2	1.06	0.41	1.12	16.1	4.5
4	87	10	3	1.60	0.61	0.86	17.4	3.2
5	79	18	3	1.23	0.56	1.09	14.1	5.6
6	85	12	3	1.20	0.61	0.97	15.3	4.3
7	92	6	2	2.17	0.72	1.03	16.7	3.5
8	75	21	4	1.01	0.71	1.16	14.0	4.6
9	86	11	3	1.33	0.66	0.92	15.0	4.1
10	91	7	2	2.81	0.78	0.90	15.6	3.4

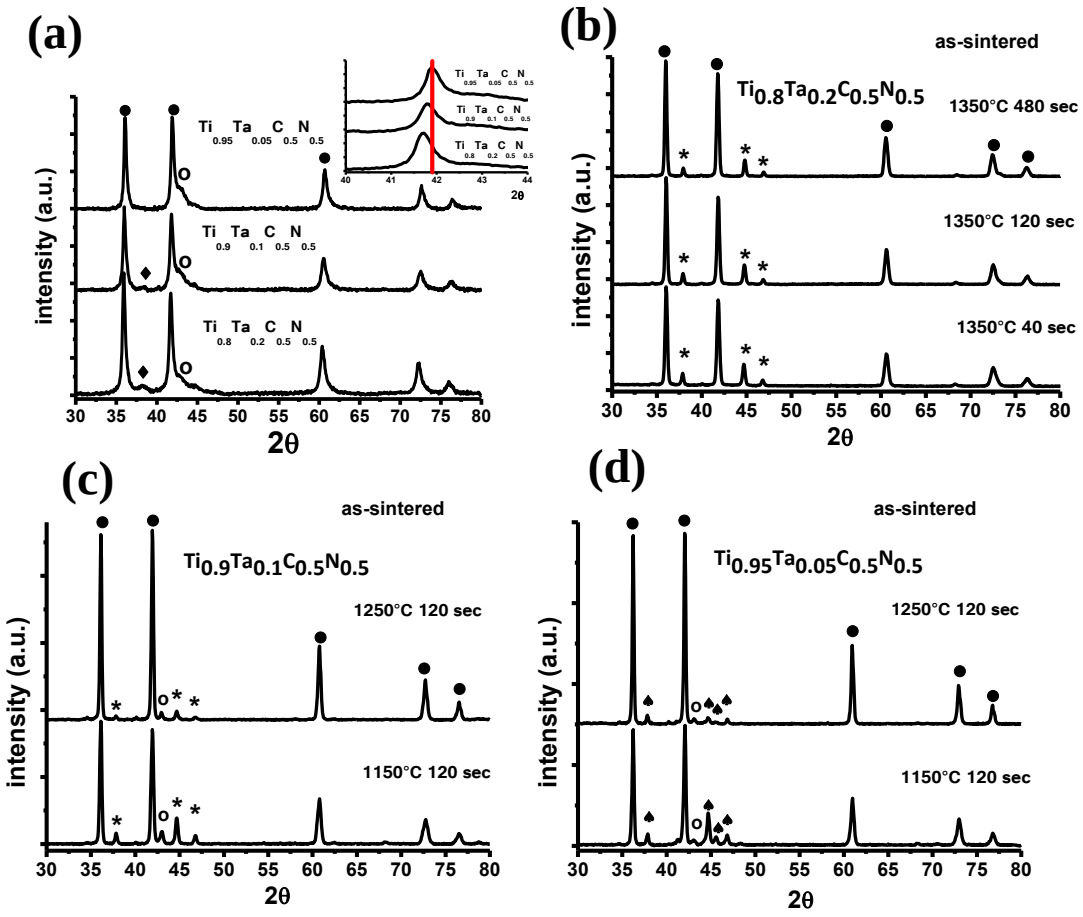
(a)
Ti Ta C N
0.95 0.05 0.5 0.5
Ti Ta C N
0.9 0.1 0.5 0.5
Ti Ta C N
0.8 0.2 0.5 0.5
intensity (a.u.)
2θ
(b)
as-sintered
Ti0.8Ta0.2C0.5N0.5
1350°C 480 sec
1350°C 120 sec
1350°C 40 sec
intensity (a.u.)
2θ
(c)
as-sintered
Ti0.9Ta0.1C0.5N0.5
1250°C 120 sec
1150°C 120 sec
intensity (a.u.)
2θ
(d)
as-sintered
Ti0.95Ta0.05C0.5N0.5
1250°C 120 sec
1150°C 120 sec
intensity (a.u.)
2θ

Figure 1

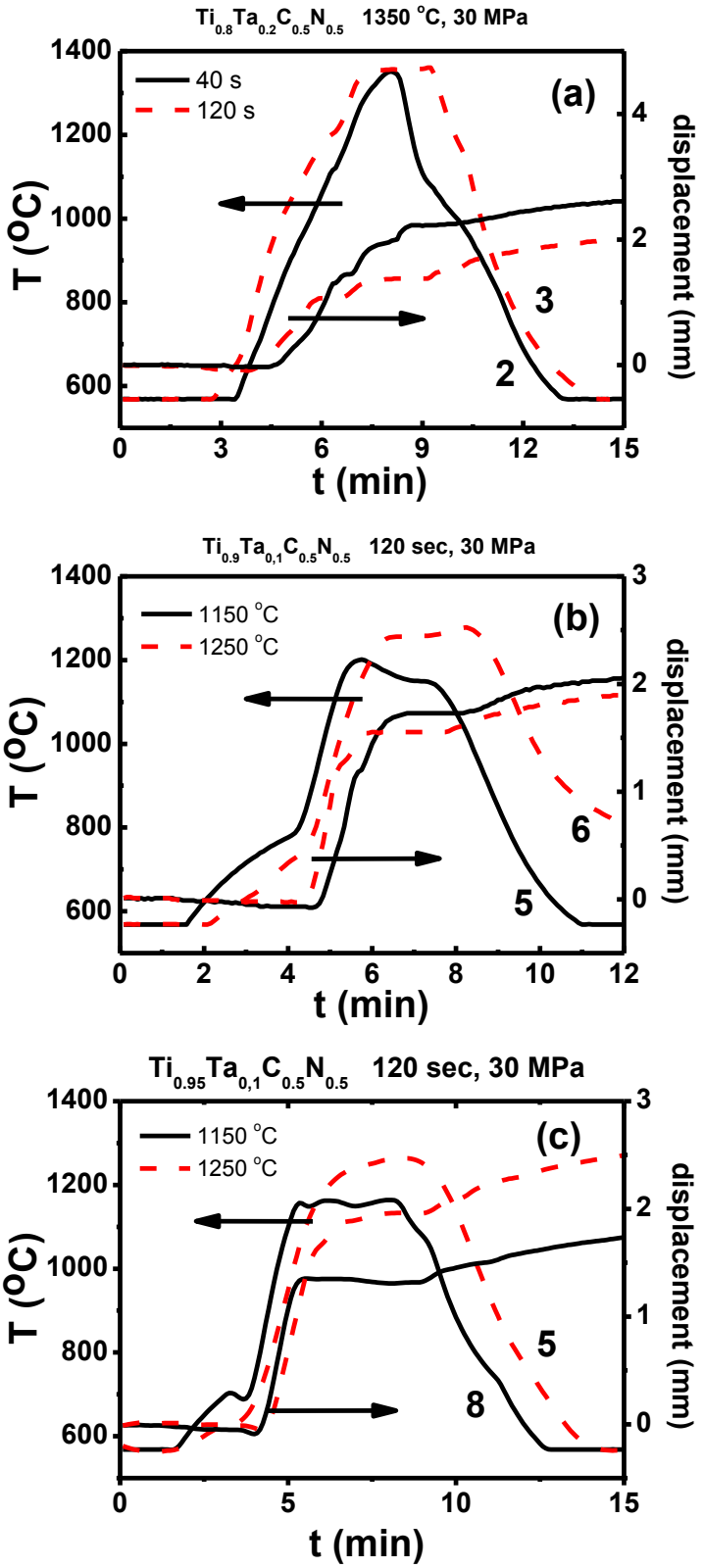
Ti0.8Ta0.2C0.5N0.5 1350 °C, 30 MPa
40 s
120 s
(a)
T (°C)
displacement (mm)
t (min)
3
2
Ti0.9Ta0,1C0.5N0.5 120 sec, 30 MPa
1150 °C
1250 °C
(b)
6
5
Ti0.95Ta0,1C0.5N0.5 120 sec, 30 MPa
(c)
5
8

Figure 2

(a) Low Magnification Images

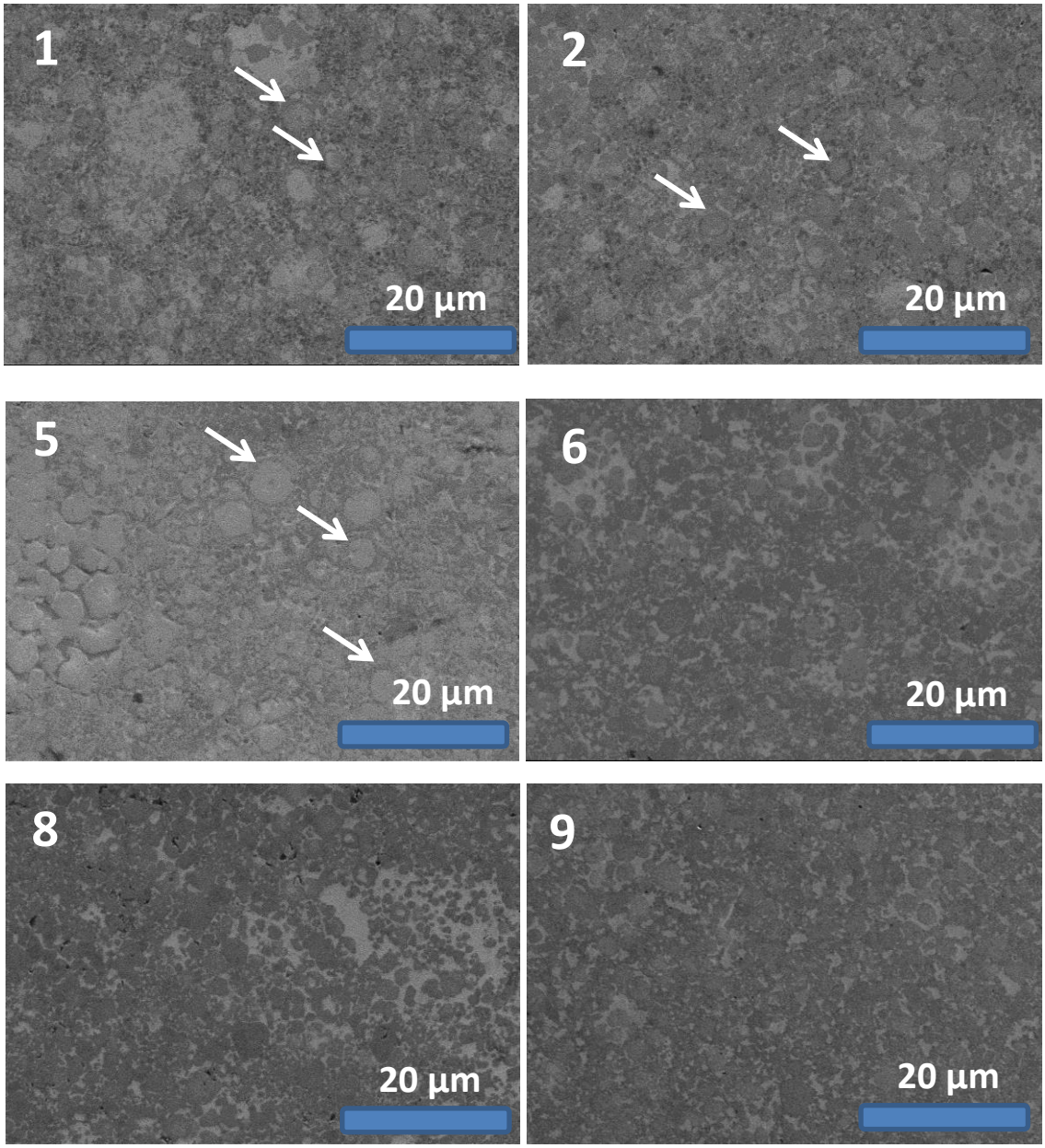

(b) High Magnification Images

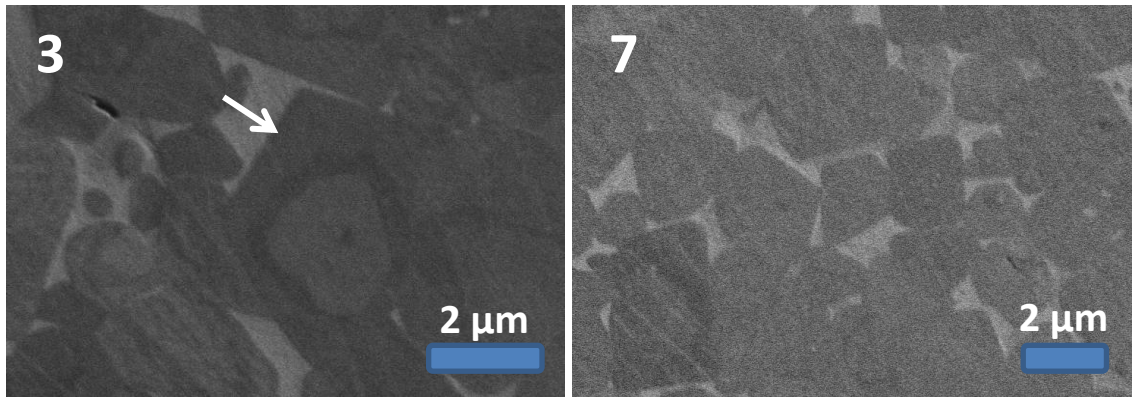

Figure 3

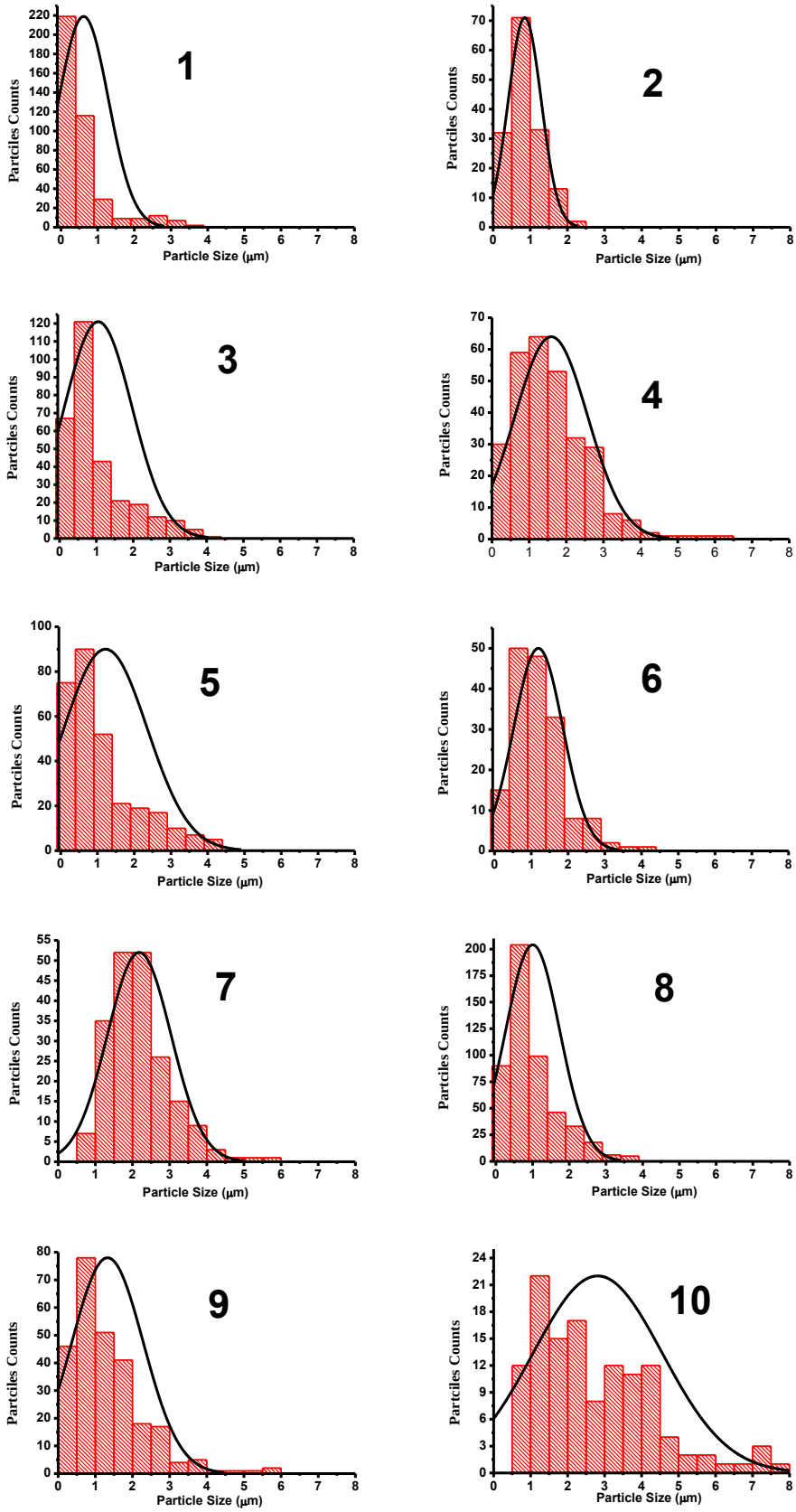

Figure 4

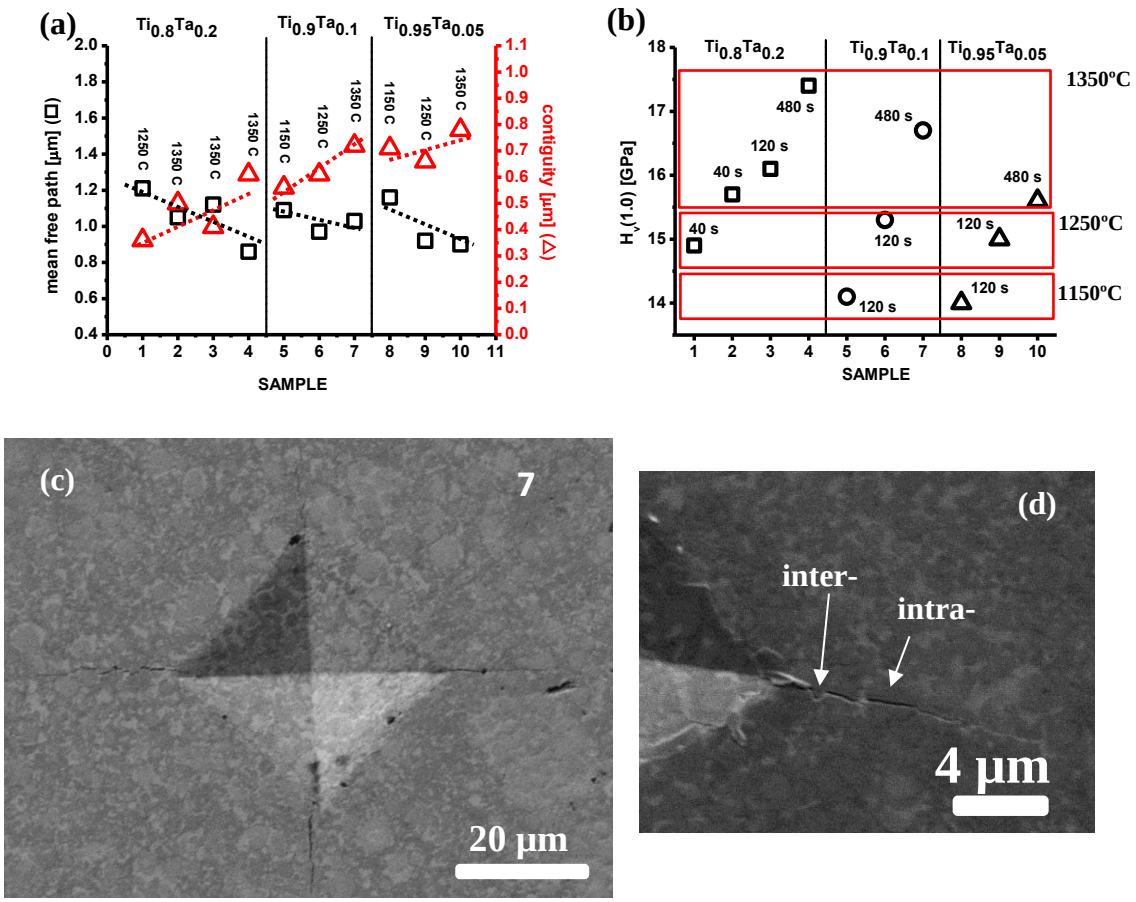
(a)
Ti0.8Ta0.2
Ti0.9Ta0.1
Ti0.95Ta0.05
mean free path [μm] (□)
contiguity [μm] (△)
SAMPLE
1250 C
1350 C
1150 C
(b)
Hv (1.0) [GPa]
480 s
120 s
40 s
1350°C
1250°C
1150°C
SAMPLE
(c)
7
20 μm
(d)
inter-
intra-
4 μm

Figure 5

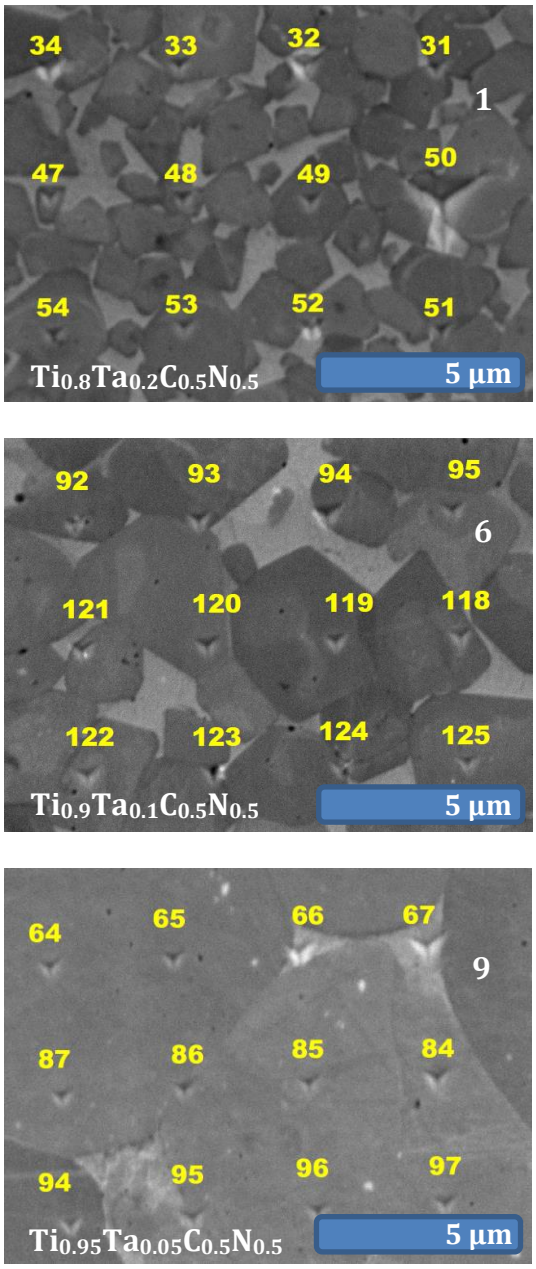
34
33
32
31
1
47
48
49
50
54
53
52
51
Ti0.8Ta0.2C0.5N0.5
5 µm
92
93
94
95
6
121
120
119
118
122
123
124
125
Ti0.9Ta0.1C0.5N0.5
5 µm
64
65
66
67
9
87
86
85
84
94
95
96
97
Ti0.95Ta0.05C0.5N0.5
5 µm

Figure 6

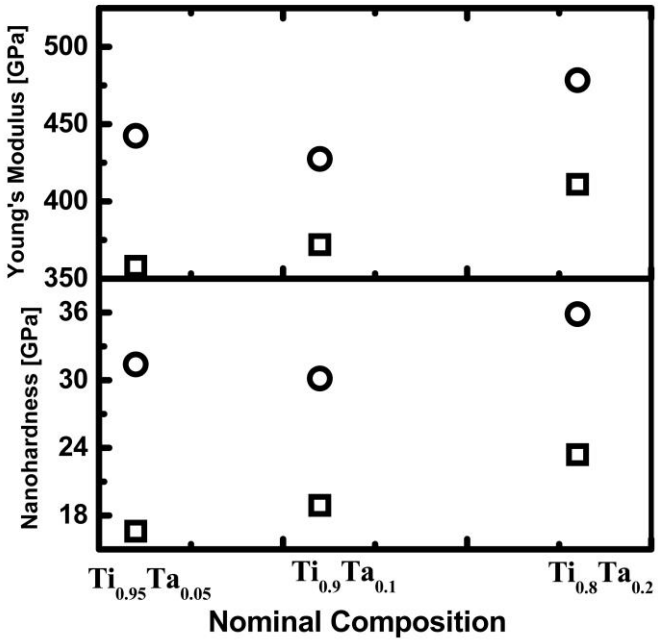
Young's Modulus [GPa]
500
450
400
350
Nanohardness [GPa]
36
30
24
18
Ti0.95Ta0.05
Ti0.9Ta0.1
Ti0.8Ta0.2
Nominal Composition

Figure 7